RESEARCH ARTICLE

Glioblastoma Cortical Organoids Recapitulate Cell-State Heterogeneity and Intercellular Transfer

Vamsi Mangena[1,2], Rony Chanoch-Myers[3], Rafaela Sartore[2,4], Bruna Paulsen[2,4], Simon Gritsch[1,2], Hannah Weisman[1,2], Toshiro Hara[1,2], Xandra O. Breakefield[5,6], Koen Breyne[5], Aviv Regev[2,7], Kwanghun Chung[8,9], Paola Arlotta[2,4], Itay Tirosh[3], and Mario L. Suvà[1,2]

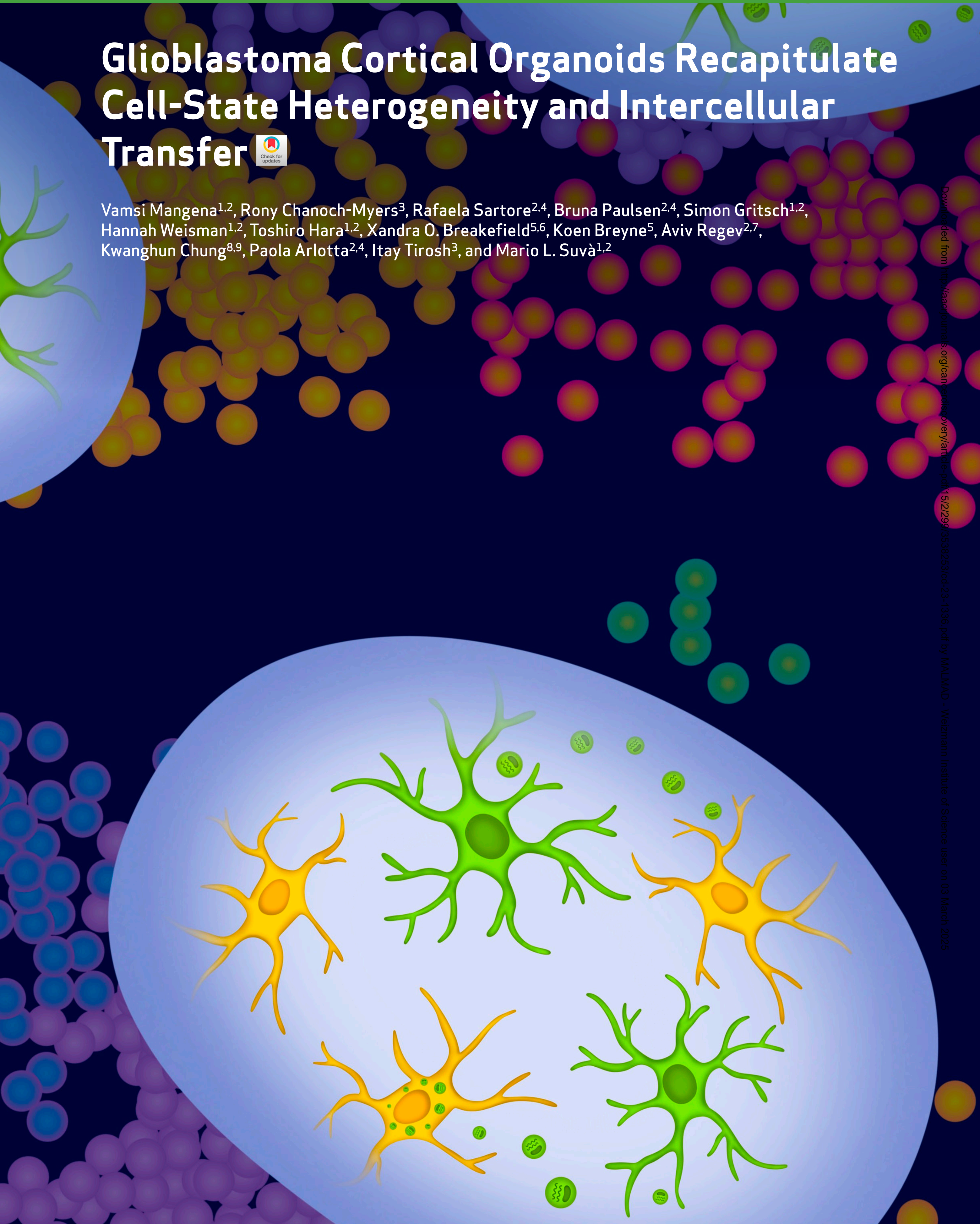

ABSTRACT

Glioblastoma (GBM) is characterized by heterogeneous malignant cells that are functionally integrated within the neuroglial microenvironment. In this study, we model this ecosystem by growing GBM into long-term cultured human cortical organoids that contain the major neuroglial cell types found in the cerebral cortex. Single-cell RNA sequencing analysis suggests that, compared with matched gliomasphere models, GBM cortical organoids more faithfully recapitulate the diversity and expression programs of malignant cell states found in patient tumors. Additionally, we observe widespread transfer of GBM transcripts and GFP to nonmalignant cells in the organoids. Mechanistically, this transfer involves extracellular vesicles and is biased toward defined GBM cell states and astroglia cell types. These results extend previous GBM organoid modeling efforts and suggest widespread intercellular transfer in the GBM neuroglial microenvironment.

SIGNIFICANCE: Models that recapitulate intercellular communications in GBM are limited. In this study, we leverage GBM cortical organoids to characterize widespread mRNA and GFP transfer from malignant to nonmalignant cells in the GBM neuroglial microenvironment. This transfer involves extracellular vesicles, may contribute to reprogramming the microenvironment, and may extend to other cancer types.

See related commentary by Shakya et al., p. 261

INTRODUCTION

Glioblastoma (GBM) is an aggressive and incurable malignancy (1). Single-cell genomic studies have highlighted extensive intratumor heterogeneity in GBM, providing a fundamental basis for the observed clinical challenges (2–6). Malignant GBM cells recapitulate at least four main cellular states: neural progenitor cell–like (NPC-like), oligodendrocytic progenitor cell–like (OPC-like), astrocytic-like (AC-like), and mesenchymal-like (MES-like; ref. 3). Importantly, these GBM cell subsets are thought to have varied functional contributions to intratumor biology (3–5, 7–10). NPC-like and OPC-like cells are thought to be primarily responsible for brain invasion and electric interaction with the neuronal microenvironment (7, 10), whereas AC-like and MES-like cells form cancer cell interconnected microtube networks and further communicate with nonmalignant cells in the tumor microenvironment (TME; refs. 7, 9, 11, 12).

Deciphering the functional role of malignant cell heterogeneity in GBM requires scalable experimental models that faithfully recreate cell states and their interactions with the human TME and can be manipulated in the laboratory. Whereas patient-derived tumor xenografts are a cornerstone of GBM modeling, these models are time- and labor-intensive and have limitations due to species mismatch (13). Conversely, *in vitro* cell cultures have enabled rapid and detailed studies in human models, but the lack of a structured neuronal microenvironment limits their capacity to model complex interactions (14). Recently, multiple human organoid–based approaches for studying GBM have emerged to address these limitations. One approach has involved growing tumor organoids from explant patient tissue; although these GBM organoids initially retain remarkable fidelity to human tumors, they contain limited neuroglial cell types and are somewhat limited by interorganoid heterogeneity and by changes in the TME over passages (15, 16). A second approach has involved grafting GBM cells into independently derived human organoids of neural origin (17, 18). Although important technical milestones have been achieved using this strategy, studies have focused on the characterization of malignant cell populations while providing limited characterization of the precise cellular compositions of the neural organoids and of the interactions between GBM and the neural organoids (8, 19–24).

---

[1]Department of Pathology and Krantz Family Center for Cancer Research, Massachusetts General Hospital and Harvard Medical School, Boston, Massachusetts. [2]Broad Institute of Harvard and MIT, Cambridge, Massachusetts. [3]Department of Molecular Cell Biology, Weizmann Institute of Science, Rehovot, Israel. [4]Harvard University, Cambridge, Massachusetts. [5]Molecular Neurogenetics Unit, Department of Neurology, Massachusetts General Hospital, Harvard Medical School, Boston, Massachusetts. [6]Department of Radiology, Center for Molecular Imaging Research, Massachusetts General Hospital and Program in Neuroscience, Boston, Massachusetts. [7]Genentech, South San Francisco, California. [8]MIT Department of Chemical Engineering, Cambridge, Massachusetts. [9]Picower Institute for Learning and Memory, Cambridge, Massachusetts.

V. Mangena and R. Chanoch-Myers contributed equally to this article.

P. Arlotta, I. Tirosh, and M.L. Suvà jointly supervised this article.

Corresponding Authors: Mario L. Suvà, Department of Pathology, Massachusetts General Hospital, 149 13th street (6010), Charlestown, MA 02129. E-mail: Suva.Mario@mgh.harvard.edu; Itay Tirosh, Department of Cell Biology, Weizmann Institute, Ullmann Building Room 135, Rehovot 7610001, Israel. E-mail: Itay.tirosh@weizmann.ac.il; and Paola Arlotta, Harvard Department of Stem Cell and Regenerative Biology, Sherman Fairchild Building, 7 Divinity Avenue, Cambridge, MA 02138. E-mail: paola_arlotta@harvard.edu

Cancer Discov 2025;15:299–315

doi: 10.1158/2159-8290.CD-23-1336

In this study, we address these limitations and describe patient-derived GBM cells and their engraftment into long-term cultured human cortical organoids (25) that have a reproducible, expanded, and well-characterized diversity of neuronal and glial subtypes, including astroglia. Direct comparison with patient-matched gliomasphere models suggests that GBM cortical organoid (GCO) models more faithfully recreate the spectrum of expression cell states observed in patient tumors. Single-cell genomic analysis of GCOs further reveals widespread transfer of endogenous malignant transcripts to nonmalignant cells in the organoid microenvironment. This transfer is biased toward defined malignant GBM cell states and astroglia cell types and is mediated at least in part by extracellular vesicles (EV). Collectively, our results advance human GBM organoid models, reveal the prevalence, extent, and pattern of mRNA transfer in the GBM microenvironment, and may extend to other tumor organoid models.

RESULTS

Establishment of GCO Models

To develop GCO models, we engrafted GFP or tdTomato (tdT)-tagged patient-derived gliomaspheres into human cortical organoids (after 4–6 months in culture; ref. 25) and allowed the joint cultures to grow for 2 weeks after engraftment (Fig. 1A; “Methods”). At 4 to 6 months, human cortical organoids reproducibly present a diversity of neuronal and glial cell types found in the normal human cerebral cortex (25) while largely avoiding the neural degeneration seen with prolonged *in vitro* culture. By 2 weeks after implantation, GFP-labeled GBM cells efficiently infiltrated and colonized within human cortical organoids, forming classical structures, such as tumor microtubes and EVs (Fig. 1B). Using an orthogonal CellTracker labeling strategy for GBM cells, we observed long-range and extensively interconnected dye-labeled networks just 4 days after implantation into cortical organoids (Fig. 1C; “Methods”). Together, these results highlight the extent to which malignant cells are readily integrated into the organoid microenvironment.

Single-Cell Genomics Characterization Shows Reproducible GCO Models

To comprehensively assess the cell-type and -state composition of the established GCO models, we dissociated the organoids and separately profiled FACS-purified GFP/tdT-positive (GFPpos) and -negative (GFPneg) cells using droplet-based single-cell RNA sequencing (scRNA-seq; Fig. 1A, D–G; Supplementary Fig. S1A). For each experiment, we dissociated an age/batch-matched nonengrafted cortical organoid as a negative control for setting reliable GFP/tdT FACS gates (Supplementary Fig. S1A). We retained 45,394 high-quality single-cell profiles across nine independent GCO models, combining different induced pluripotent or embryonic stem (iPS/ES) cell lines and tumor source cells (Fig. 1D and F; Supplementary Table S1). We robustly categorized cells as malignant or nonmalignant based on an established computational approach for inference of copy-number alterations (CNA) from single-cell profiles (26) using GFPneg nonmalignant cells as a CNA reference (Fig. 1E and H; Supplementary Fig. S1B). Across all models, GFPpos malignant cells grouped separately by patient in a low-dimensionality embedding with Uniform Manifold Approximation and Projection (UMAP), whereas nonmalignant cells grouped by cell type and not individuals, as seen in previous single-cell studies (Fig. 1D-E, I; ref. 3).

The profiles of nonmalignant, cortical organoid–derived cells partitioned by major cortical cell classes and were annotated with an established cell type naming convention (25, 27) as corticofugal projection neurons, callosal projection neurons, intermediate progenitors, immature interneurons, outer radial glia (oRG) and/or astroglia, and apical radial glia (Fig. 1I; Supplementary Fig. S1C and S1D; Supplementary Table S2). Although the cortical organoids used for model establishment were derived from three different human donor iPS/ES cell lines, all major cortical cell classes were broadly present across individual experiments and lines (Fig. 1I and J; Supplementary Fig. S1C and S1D; “Methods”), albeit with slight deviations in cell type representation, likely due to the variable age of the cortical organoids at the time of GBM implantation (within a 4–6 months range). These findings are consistent with previously described maturation trajectories of cortical organoids over time (25).

Malignant Cell States in GCOs Mirror Human Tumors and Are Impacted by the Organoid Microenvironment

Examining the malignant compartment of GCO models, we analyzed 7,658 malignant cell profiles (by CNA-based classification) from the nine GCOs (Fig. 1D and E; Supplementary Table S1). We characterized the expression programs in these cells by first applying nonnegative matrix factorization (NMF) to the profiles from each model separately and then comparing the resulting programs across all established models, as previously described (Fig. 2A; Supplementary Fig. S2A; Supplementary Table S3; refs. 28, 29).

Six major programs recurred in two or more models (Fig. 2A), with direct mapping between the GCO programs and canonical GBM cell states from human tumors [Fig. 2A (bottom); ref. 3]. Overall, GCO models contained cell subsets expressing an NPC-like program, AC-like program, two MES-like programs, a cell-cycle program, and an OPC-like program, the last of which had not been previously detected in the gliomasphere models that were used in the current study but was observed when those same cells were placed in the GCO context (Fig. 2B; Supplementary Fig. S2B), highlighting the strength of the GCO model.

We next examined the effect of the organoid microenvironment on malignant cell states by scoring individual malignant cells from each GCO and patient-matched *in vitro* gliomasphere model for the canonical human GBM programs (Fig. 2B; Supplementary Fig. S2B). For many of the models, the number of cells that were confidently assigned to one of the GBM states, as well as the magnitude of observed cell state scores of assigned cells, was significantly higher in the GCO context, suggesting that cortical organoids have the potential

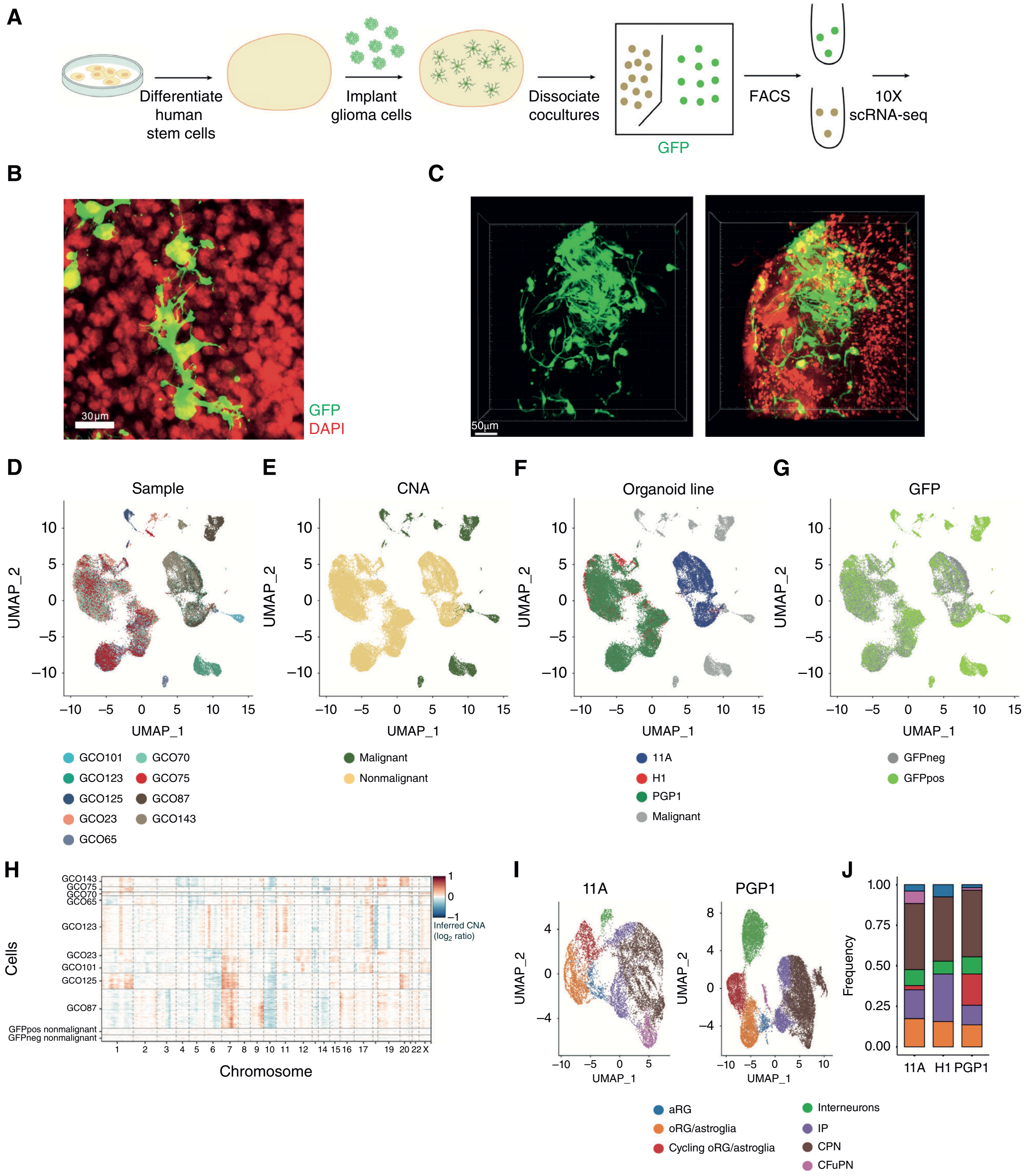

Figure 1. Establishment and cellular diversity of GCOs. **A,** Experimental schematic for establishment and scRNA-seq of GCOs. **B,** Confocal maximum intensity projection of GFP-tagged MGH143 GBM cells grown in 11A-derived cortical organoids. GFPpos cells are shown in green, with DAPI-stained nuclei in red. **C,** Confocal 3D image reconstruction of CellTracker dye-labeled MGH143 GBM cells allografted in cortical organoids. Dye-labeled cells are shown in green, with DAPI-stained nuclei in red. **D–G,** scRNA-seq: UMAP visualization of single cells from GCOs annotated by the (**D**) GCO model (defined by the GBM cell line), (**E**) CNA status, (**F**) iPS/ES stem cell line, and (**G**) GFP-sorting compartment. **H,** Inferred CNA profiles of malignant cells derived from GCOs. GFPneg nonmalignant cells were used as a reference. A representative population of GFPpos cells lacking malignant CNA signatures is annotated as an example. **I,** UMAP visualization of nonmalignant cells from 11A-derived (~4–5 months old) and PGP1-derived (~5–6 months old) GCOs. **J,** Bar plot showing the relative abundance of nonmalignant cell types across humanized GCO models for all iPS/ES stem cell lines. aRG, apical radial glia; CPN, callosal projection neurons; CFuPN, corticofugal projection neurons; DAPI, 4′,6-diamidino-2-phenylindole; IP, intermediate progenitors; oRG/astroglia, outer radial glia and/or astroglia.

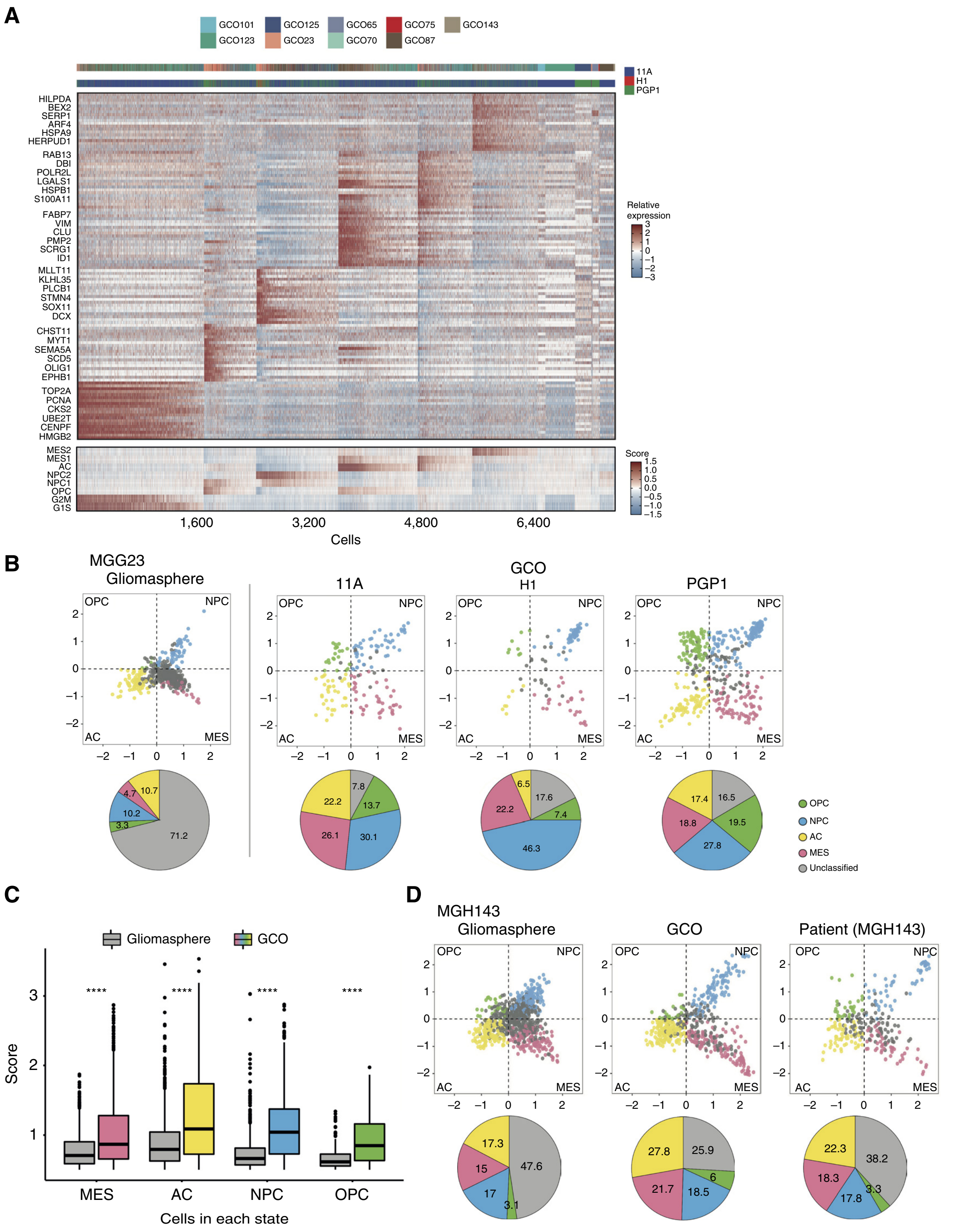

Figure 2. Malignant cell states in GCOs. **A,** Programs of heterogeneity identified using NMF in malignant cells from GCOs. Top, annotation bars colored by the GBM cell line (top) or organoid-associated iPS/ES cell line (bottom). Middle, Heatmap shows relative expression of genes from six programs across all cells. Bottom, Heatmap shows relative scores of the canonical GBM cellular states, as defined previously [Neftel and colleagues (3)]. **B,** Two-dimensional "star" representation of cellular states for malignant cells derived from the MGG23 GBM cell line. Each quadrant corresponds to one cellular state, as defined previously [Neftel and colleagues (3)]. Left, gliomasphere model. Right, GCO model, shown for each iPS/ES cell line used to generate cortical organoids. Colors correspond to states: OPC–green, NPC–blue, AC–yellow, MES–pink, and unclassified cells in gray. Bottom, Pie charts quantifying the cells in each state from the "star" plots. **C,** Boxplots quantifying GBM program scores in malignant cells across all human models, with comparison of patient-matched gliomaspheres (gray) or GCOs (colored). (****, $P < 10^{-22}$ in comparisons by *t* test). **D,** Two-dimensional "star" representation of cellular states for malignant cells derived from the MGH143 tumor/cell line. Colors correspond to states: OPC–green, NPC–blue, AC–yellow, MES–pink, and unclassified cells in gray. Left: Gliomasphere model, Middle: GCO model, Right: Patient tumor [Neftel and colleagues (3)]. Bottom, Pie charts quantifying the cells in each state from the "star" plots.

to induce cell states that are more representative of those seen in human tumors (Fig. 2B and C; Supplementary Fig. S2B and S2C; $P < 10^{-16}$, t test). Accordingly, we further found that malignant cells in the GCO143 model more closely resembled tumor cell state scores from the originating (MGH143) patient tumor (3) compared with gliomasphere conditions (Fig. 2D; Supplementary Fig. S2D). Importantly, the GBM cell state composition in GCO23 models derived from three different human stem cell lines was comparable, highlighting that the GCO effect is not idiosyncratic to the originating iPS/ES cell line but reproducible across lines (Fig. 2B).

To further dissect the impact of the cortical organoid microenvironment on malignant cells, we identified differentially expressed genes between patient-matched GCO and gliomasphere models grown *in vitro* (Supplementary Fig. S2E and S2F). Malignant cells in organoids most strongly upregulated neuronal genes, whereas malignant cells in gliomaspheres upregulated cell-cycle genes (Supplementary Fig. S2E and S2F). We further observed that eight of the nine GCOs had a reduction in the proportion of cycling cells compared with patient-matched gliomaspheres (Supplementary Fig. S2G). These results are in line with neuronal states being more dependent on the microenvironment and possibly enriched in the infiltrative compartment of tumors (7). Moreover, the reduction of cycling cells in the organoid context would be analogous to human tumors, which typically have a lower percentage of cycling cells than observed for derived cell lines *in vitro* (30). Finally, we compared cortical organoids to cerebral organoids using a previously published dataset (23) and found that there was minimal qualitative difference in the extent and pattern of GBM cell state modeling (Supplementary Fig. S2H).

GCOs Model a GFP Transfer Process from Malignant to Nonmalignant Cells

We next considered the nonmalignant compartment of GCOs. Because GBM cells stably expressed GFP/tdT (from lentiviral vectors) prior to implantation in unlabeled cortical organoids, we anticipated that sorting cells by GFP/tdT expression would cleanly separate malignant and nonmalignant populations. Whereas malignant cells were only found in the GFPpos compartment across all experiments, we were surprised to find a significant number of nonmalignant cells (defined by lack of CNAs and having nonmalignant expression profiles) in both the GFPneg and GFPpos compartments (Fig. 1D–G; Supplementary Fig. S1B). In particular, 14,625 of a total of 37,736 nonmalignant cells (38.8%) were defined as positive for GFP protein expression by FACS.

To better understand the origin of GFPpos nonmalignant cells, we compared the FACS profile of the MGG23-GFP/H1 GCO to reference populations, including the unengrafted H1 cortical organoid and the pure MGG23-GFP cell line (Fig. 3A; Supplementary Fig. S3A). The GCO had very-high–expressing GFPpos cells that were overlapping with the pure MGG23-GFP cell line, as well as a population of intermediate-expressing GFPpos cells that were distinct from the GFPneg H1 organoid population used as a negative control. These results corroborated the emergence of a *de novo* GFPpos population of cells in GCOs that likely represents nonmalignant cells.

We verified the presence of GFPpos nonmalignant cells using an orthogonal approach by counting the number of GFP/tdT lentiviral sequences in the single-cell transcriptomes from all GCOs (Fig. 3B and C; Supplementary Fig. S3B and S3C). In addition to malignant cells that had GFP transcripts detected at significantly higher levels than all nonmalignant cells ($P < 10^{-16}$, t test), ~17% of GFPpos nonmalignant cells (2,399/13,374) had detected GFP transcripts, whereas this was a much smaller fraction (0.43%) in GFPneg nonmalignant cells. This concordance between the protein (from FACS) and RNA (from scRNA-seq) levels eliminates the possibility that this population was due to either a sorting error or ambient RNA. Furthermore, we reproduced these results across multiple plate-based scRNA-seq (SMART-Seq2) assays, in which ambient RNA is far less prevalent (Supplementary Fig. S3C), further supporting our conclusions. Lower detection rates for the tdT transcripts prevented analogous validations of tdT transfer (Supplementary Fig. S3D).

As additional verification, we performed immunofluorescence confocal imaging in a mixed-species GCO model in which we engrafted GFP-labeled mouse (m005-GFP) GBM cells into human cortical organoids. We stained the tissue with an antibody labeling human-specific mitochondria and observed colocalization with GFP protein, providing further validation for GFP transfer from mouse malignant cells to nonmalignant human cells (Fig. 3D). Critically, the colocalization was most pronounced in areas of low GFP expression, consistent with our previous results showing reduced GFP transcripts and protein in GFPpos nonmalignant cells compared with GFPpos malignant cells (Fig. 3A–C).

We next explored whether malignant cells may be fusing with nonmalignant cells. We observed that the CNA profiles of GFPpos nonmalignant cells were indistinguishable from those of GFPneg nonmalignant cells and distinct from those of malignant cells from the same model (Fig. 1H; Supplementary Fig. S1B). In line with this, GFPpos and GFPneg nonmalignant cells cluster closely together by their expression profiles, whereas malignant cells cluster separately (Fig. 1D–G). Thus, our findings suggest a biological process that involves a relatively small amount of material transfer from malignant to nonmalignant cells, whereby the overall identity of nonmalignant cells is unchanged in the short term. We then considered the cell type specificity of GFP transfer to nonmalignant cells. Although all nonmalignant cell types were implicated as "recipients" of GFP transfer in GFP-based models (Supplementary Fig. S3B, S3D, and S3E), the GFPpos compartment was relatively enriched in the oRG/astroglia population (Fig. 3E; $P < 0.001$, permutation test). This finding is concordant with astroglia functions in communication and molecular uptake in the brain and in synaptic microenvironments (31).

Widespread Transfer of mRNA Transcripts in GCOs

We next hypothesized that endogenous mRNAs, aside from GFP, may also be transferred from malignant to nonmalignant cells. To test this hypothesis, we leveraged our mixed-species experimental model (mouse GBM m005-GFP grown in human cortical organoids). We sorted cells into GFPpos and GFPneg populations and analyzed them by scRNA-seq. We aligned the

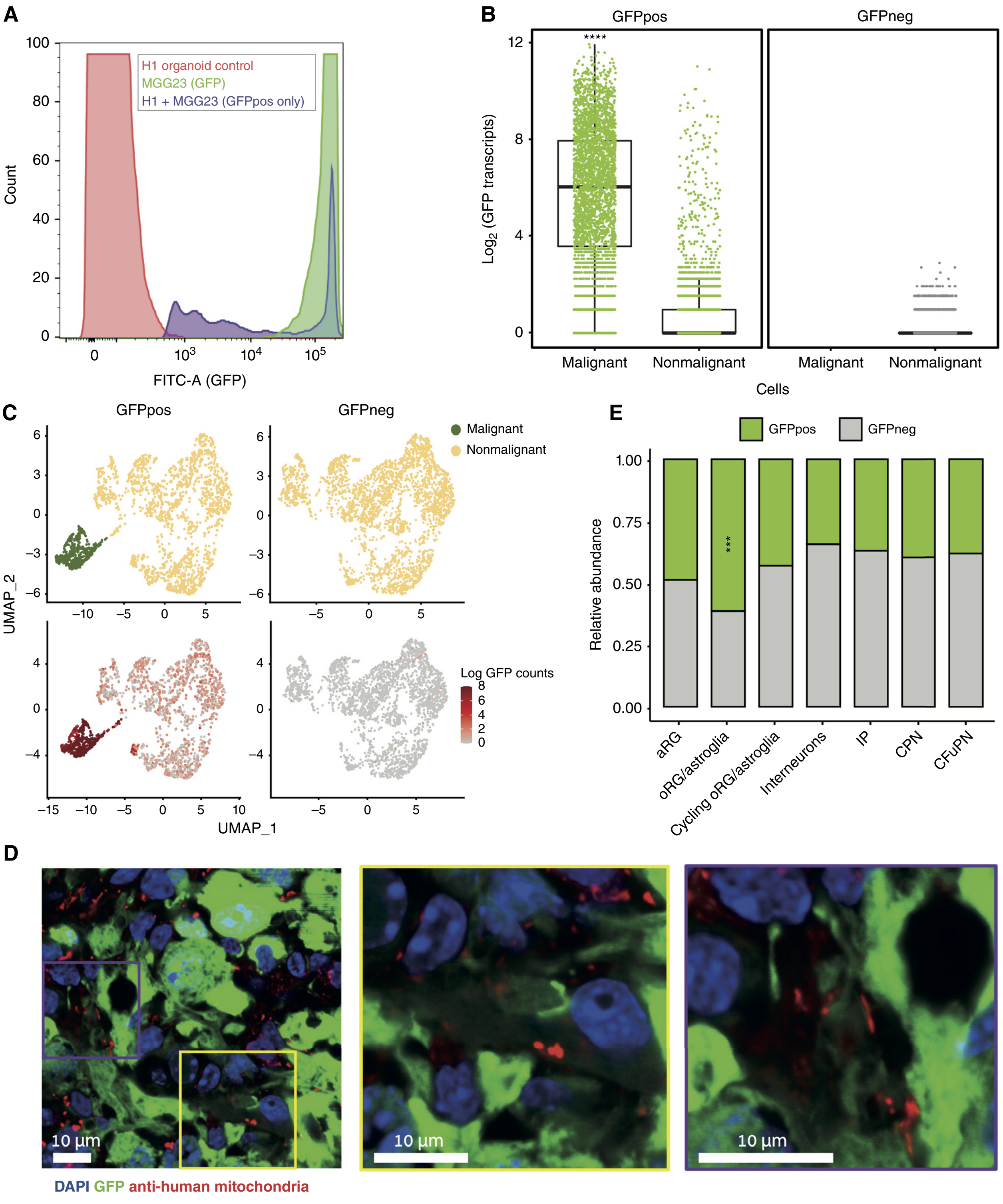

Figure 3. GCOs model a GFP transfer process. **A,** FACS histogram plot showing GFP protein expression for (i) cells from unlabeled H1 cortical organoids only (red), (ii) MGG23-GFP cells only (green), and (iii) GFPpos cells isolated from H1 + MGG23-GFP (GCO23) models (purple). **B,** Detected GFP transcripts from (10x-based) scRNA-seq for all human GCOs. Cells were grouped by malignant classification and GFP protein expression (defined by FACS gates). (****, $P < 10^{-22}$ in comparisons by *t* test). **C,** UMAP visualization of all GFPpos (left) and GFPneg (right) cells from GCO143. Cells are colored by malignant status (top) and GFP transcript counts (bottom). **D,** Immunofluorescence staining and confocal imaging of thin sections (~15 microns) of m005-GFP GCOs. Purple and yellow boxes (left) delineate magnified regions (center: yellow, right: purple). **E,** Bar plot showing the relative abundance of GFPpos and GFPneg cells for each nonmalignant cell type across all human GCOs. (***, $P < 0.001$ in comparisons by the permutation test, in which the fraction of times the real fraction of GFPpos cells was higher than a shuffled group of cells of that size over 1,000 iterations). aRG, apical radial glia; CPN, callosal projection neurons; CFuPN, corticofugal projection neurons; DAPI, 4′,6-diamidino-2-phenylindole; IP, intermediate progenitors; oRG/astroglia, outer radial glia and/or astroglia.

sequencing reads to a joint mouse and human transcriptome, readily classifying mouse and human cells (Fig. 4A; Supplementary Fig. S4A). Cells with high read counts for both mouse and human genes were discarded as suspected doublets (see "Methods"), and the remaining cells were clustered and visualized in a low-dimensionality UMAP embedding (Fig. 4B). Mirroring our results from the all-human GCOs, the malignant mouse cells were only found in the GFPpos compartment, whereas the nonmalignant human cells were found in both the GFPpos and GFPneg compartments (compare Fig. 4B to Fig. 1D–G). Moreover, we found a consistent spectrum of nonmalignant cell types across the mouse and human experiments [compare Fig. 1I to Fig. 4B (middle)].

We next quantified exogenous GFP transcripts and endogenous mouse (mm10) transcripts in both the mouse and human cells (Fig. 4C; Supplementary Fig. S4B–S4D). As expected, we observed high GFP transcript levels in the mouse cells, followed by intermediate levels in the GFPpos human cells and minimal levels in the GFPneg human cells (Fig. 4C; $P < 10^{-16}$, *t* test). The GFP transcript levels were highly correlated with mouse transcript detection. Thus, the GFPpos human cells had detection of mouse transcripts ($P < 10^{-22}$, *t* test) at levels significantly higher than the GFPneg human cells but at lower levels than the mouse cells (Fig. 4C; Supplementary Fig. S4C and S4D). Together, these results show orthogonal validation of GFP transfer using a CNA-independent cell classification system and reveal that this transfer extends from GFP to a significant number of endogenous transcripts.

We next explored the identities of endogenous transcripts transferred from malignant to nonmalignant cells, particularly in the context of the global malignant cell transcriptome. Using the mouse (m005) GCO model (Supplementary Fig. S4E; Supplementary Table S4), we observed a highly positive correlation ($R = 0.89$; $P < 10^{-16}$) between the expression levels of mouse genes in malignant mouse cells and their levels in GFPpos (but not GFPneg) human nonmalignant cells (Fig. 4D and E; Supplementary Fig. S4F). These results suggest that the transcripts transferred from malignant to nonmalignant cells reflect random sampling of the entire malignant transcriptome. Interestingly, these global trends were maintained when each of the nonmalignant cell types was considered individually (Supplementary Fig. S4F), indicating that the driving force for material transfer is largely intrinsic to the malignant cells.

We subsequently sought to evaluate whether transfer of the malignant transcriptome was also evident in the all-human GCOs. In contrast to the species-mixing experiments, in this case, we were unable to leverage a straightforward method for high-confidence identification of the cell type origin (e.g., malignant vs. nonmalignant) for individual transcripts. We instead defined the set of 1,000 most malignant-enriched genes, compared with nonmalignant cortical organoid cells, and scored all nonmalignant cells for this malignant-enriched gene set (Fig. 4F and G). The GFPpos nonmalignant cells scored higher for this program compared with the analogous GFPneg cells (Fig. 4G; Supplementary Fig. S4G; $P < 10^{-9}$ by *t* test). The magnitude of this change was expectedly subtle, given that the amount of material transfer seems to be small compared with the recipient cell transcriptome and that the malignant-enriched genes still have appreciable gene expression in the cortical organoid cells (Fig. 4A and F). Importantly, there was no difference in expression when examining all profiled genes between the GFPpos and GFPneg populations (Fig. 4G; Supplementary Fig. S4G). These data support that widespread transfer of the malignant transcriptome to recipient nonmalignant cells also occurs in all-human GCO models.

Finally, we considered whether mRNAs could be transferred from nonmalignant cells to malignant cells in GCOs. In this case, we lacked a marker (i.e., GFP in nonmalignant cells) to identify malignant cells that had received mRNAs from nonmalignant cells; however, we partially circumvented this limitation by reanalyzing the scRNA-seq results from the m005 species-mismatched model. Our analysis revealed that human transcripts were found in mouse malignant cells but at significantly lower levels compared with that of nonmalignant human cells, as expected (Supplementary Fig. S4H). The expression of human genes in the mouse malignant cells was correlated with their expression in the human organoid/nonmalignant cells, similar to the expression of mouse genes in nonmalignant cells correlated to their expression in the mouse/malignant cells (Supplementary Fig. S4I). To understand which malignant cells had higher levels of detected human genes, we further classified the malignant cells into GBM states (see "Methods" and Supplementary Table S4) and examined the number of detected human reads. We found that the OPC/NPC-like mouse malignant cells exhibited the highest levels of detected human genes (Supplementary Fig. S4J), suggesting preferential mRNA transfer based on cell state.

AC/MES-like Programs Are Enriched in GCO mRNA Transfer

To determine the potential biological significance of mRNA transfer to nonmalignant cells, we identified genes that were differentially expressed between GFPpos and GFPneg nonmalignant cells of each cell type across the full cohort of human GCOs (Fig. 4H; Supplementary Fig. S4K). GFPpos nonmalignant cells highly upregulated a distinct subset of genes, whereas there was no analogous subset of downregulated genes (Fig. 4H). The genes highly upregulated in GFPpos nonmalignant cells were strongly enriched for the GBM AC-like and MES-like expression programs compared with the NPC-like and OPC-like programs (Fig. 4H; Supplementary Fig. S4L). We additionally calculated GBM program scores for all nonmalignant cell types and showed that AC-like and MES-like scores were increased across GFPpos nonmalignant cells, whereas NPC-like scores were decreased (Supplementary Fig. S4L and S4M).

We next considered the functional impact of AC/MES-like transcript transfer on nonmalignant cells. Given potential similarities between the AC/MES-like programs in GBM and nonmalignant reactive astrocyte programs, we scored nonmalignant cells for two canonical programs of astrocyte reactivity (32). We found that GFPpos oRG/astroglia had increased scores for both reactive astrocyte programs, suggesting a potential functional remodeling of defined recipient cell populations (Supplementary Fig. S4N), although determining causation remains challenging.

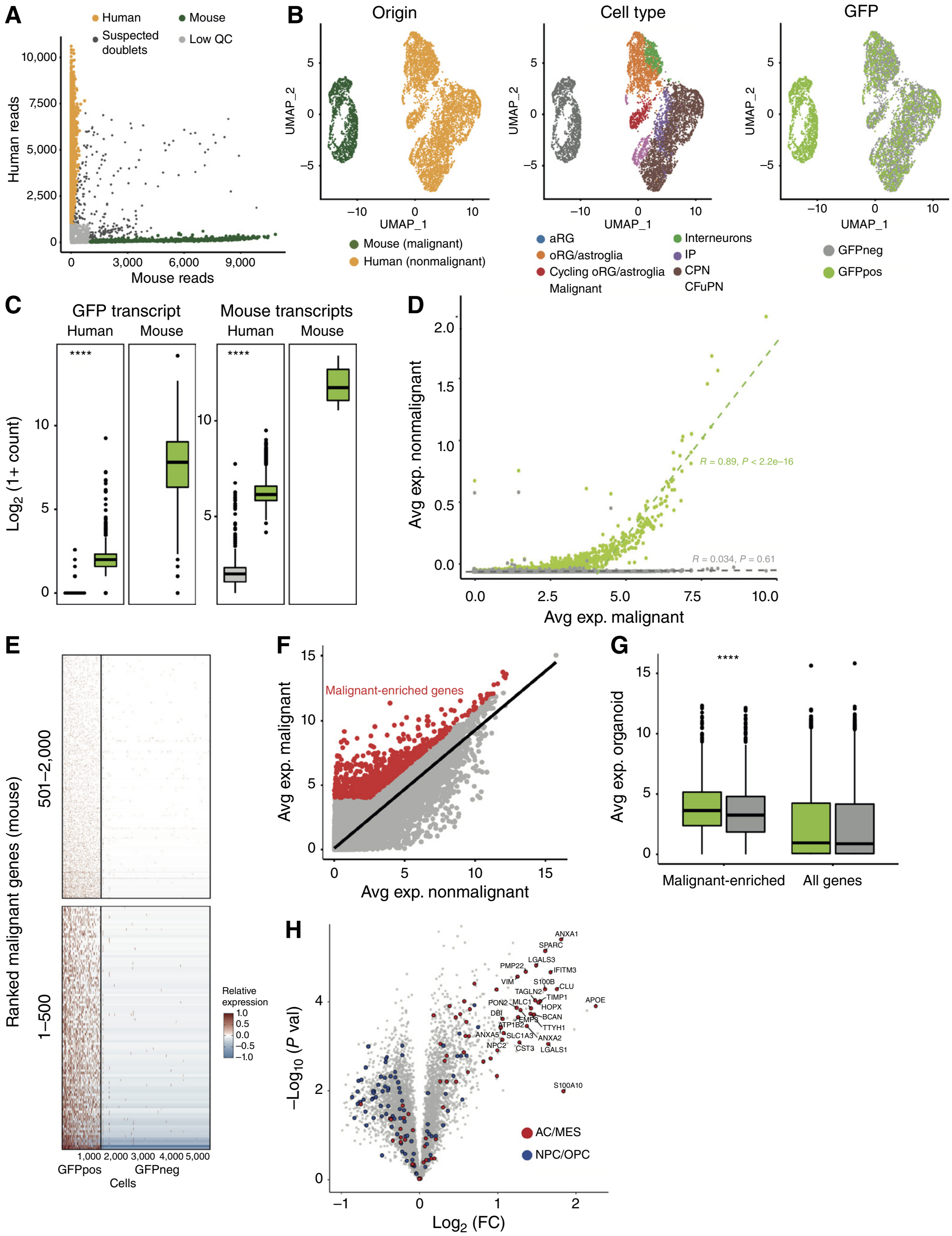

Figure 4. Widespread transfer of endogenous malignant transcripts in GCOs. **A,** Joint alignment of scRNA-seq reads from mixed-species (m005; mouse GBM–human cortical organoid) GCOs to human and mouse (mm10) reference transcriptomes. Low-quality cells (light gray) and suspected doublets (high for both mouse and human reads, dark gray) were filtered out, and the remaining cells were classified as human (orange) or mouse (green) origin. **B,** scRNA-seq: UMAP visualization of cells from mixed-species (m005) GCOs colored by species origin (left), nonmalignant cell type (center), and GFP-sorting compartment (right). **C,** Boxplots showing the transcript counts of GFP (left) or mouse genes (right) detected in the human or mouse assigned populations, colored by GFP-sorting status: GFPpos (green) and GFPneg (gray). (****, $P < 10^{-22}$ in comparisons by *t* test). **D,** Scatterplot showing average expression, for each mouse (mm10) gene, in malignant cells (*x* axis) against nonmalignant cells (*y* axis) for both GFPpos (green) and GFPneg (gray) populations. Average expression for each gene was calculated from pseudobulk scRNA-seq data of the mixed-species (m005) GCO model. The *P* value and Pearson correlation coefficient for each fitted line of genes with $\log_2(1 + \text{avg TPM})$ above 4 shown. **E,** Heatmap showing the relative expression of the first 500 (bottom) or 501–2000 (top) most highly expressed (in malignant cells) mouse (mm10) genes in all nonmalignant cells from mixed-species (m005) GCOs (left: GFPpos, right: GFPneg). **F,** Scatterplot showing the average expression of each gene in the nonmalignant cells (*x* axis) against the average expression in the malignant cells (*y* axis) calculated by pseudobulk scRNA-seq data of the human GCOs. The genes in red were defined as "malignant-enriched genes", calculated as genes with the highest residuals from the linear fit. **G,** Boxplots showing the average expression of "malignant-enriched" genes from **F** (left) or all genes (right) in nonmalignant cells from human GCOs. Boxes are colored by GFP-sorting compartments: GFPpos (green) and GFPneg (gray). (****, $P < 10^{-9}$ in comparisons by *t* test). **H,** Volcano plot illustrating differentially expressed genes between GFPpos and GFPneg nonmalignant cells from human GCOs. Individual genes are colored by their inclusion in canonical GBM expression programs: AC/MES-like (red) and NPC/OPC-like (blue). aRG, apical radial glia; Avg exp., average expression; CPN, callosal projection neurons; CFuPN, corticofugal projection neurons; FC, fold change; IP, intermediate progenitors; oRG/astroglia, outer radial glia and/or astroglia; QC, quality control; val, value.

Extracellular Vesicles Mediate Intercellular Transfer in GCOs

We hypothesized that EVs may be a mechanism of protein/mRNA transfer in GCOs. To investigate this hypothesis, we performed size-exclusion chromatography to obtain concentrated EV fractions from m005-GFP cells, MGG23-GFP cells, 11A cortical organoids, and the joint m005-11A GCO model. We characterized and quantified the EV populations by nanoparticle tracking analysis, observing that our EV preparations had mode sizes of between 140 and 160 nm (Supplementary Fig. S5A). Notably, purified EVs from MGG23-GFP cells were GFPpos under fluorescence microscopy, demonstrating that GFP proteins are packaged into EVs from GFPpos malignant cells (Fig. 5A).

To assess if mRNAs are packaged in EVs, we isolated total EV RNA from each model system and then profiled mRNAs by bulk RNA-seq. We focused on the m005-related models, such that we could align sequencing reads to the mouse transcriptome to identify malignant transcripts. We found a high correlation between malignant transcripts in EVs and transcripts expressed in malignant cells from GCOs (Fig. 5B). These results support that EVs are at least one potential mRNA transfer mechanism in GCOs and are consistent with previous reports suggesting that the RNA content in EVs is often reflective of RNA levels in the originating cell, although deviations exist (33–35). Interestingly, we found that AC/MES-like transcripts were enriched in EV mRNAs from the m005 GCO model compared with the m005 cell line alone (Fig. 5C; AC $P = 3.78\text{e}{-06}$, MES1 = 1.14e−02 by hypergeometric test), suggesting that the organoid microenvironment plays a role in promoting increased transfer of AC/MES-like transcripts.

We next performed functional assays to determine whether EVs could mediate GFP transfer in a simplified coculture setting. We cocultured human cortical organoids with either (i) conditioned media from m005-GFP cells, (ii) purified EVs from m005-GFP cells, or (iii) m005-GFP cells separated by a transwell barrier (400 nm pore size). Surprisingly, we found that after dissociating and analyzing the cortical organoids by flow cytometry, there was no evidence of GFP transfer in these cocultures, whereas the fully integrated GCO, established in parallel, had the expected GFP transfer pattern (Supplementary Fig. S5B). Although these results do not exclude a specific transfer mechanism, they highlight that the observed intercellular transfer is dependent on malignant cells being directly integrated within the TME.

We then sought to directly visualize GFP transfer patterns *in situ*. We engineered GCOs with malignant cells stably expressing palmitoylated GFP (palmGFP), a membrane-bound form of GFP that allows efficient visualization of EVs and membrane projections (36). We initially established m005-palmGFP GCOs and imaged fixed tissue sections with confocal microscopy, observing widespread GFPpos membrane projections (Fig. 5D). We observed that GFPpos vesicles were distributed within membrane projections, highlighting a potential synergistic role for membrane-based cellular connections such as tunneling nanotubes (TNT), which are known to allow transfer of large cargo (37, 38). We further carried out live confocal imaging of intact MGG23-palmGFP GCOs to mitigate the possibility of imaging artifacts due to fixation, while also assessing a fully human system (Fig. 5E). We observed similar GFPpos membrane projections in addition to an abundance of EVs distributed throughout the TME.

Transfer Extends to a Carcinoma Cortical Organoid Model

We sought to investigate the possibility that EV-mediated mRNA transfer might occur in other cancer organoid models beyond GBM. We thus developed a carcinoma cortical organoid model in which GFP-labeled breast cancer cells (MDA-MB-231) were engrafted in cortical organoids. After 2 weeks, the cultures were dissociated and flow sorted into GFPpos and GFPneg populations prior to scRNA-seq. After separating malignant and nonmalignant cells, we detected GFP transcripts in nonmalignant cortical organoid cells, supporting that transfer in organoid models occurs beyond GBM (Fig. 5F; Supplementary Fig. S5C). We further examined the GFPpos nonmalignant cells in this experiment and found that, similarly to the GCO system (Supplementary Fig. S5D), they upregulated canonical EV markers (Supplementary Fig. S5E), consistent with a model in which the identities of transferred transcripts are related to malignant cell expression (Figs. 4D and 5B).

DISCUSSION

In this study, we describe the development of GCO models for dissecting tumor heterogeneity and intercellular communication in human GBM (Fig. 6). We leveraged long-term cultured cortical organoids to achieve unprecedented cellular diversity, considering both the malignant and nonmalignant compartments, for a fully *in vitro* GBM model. The observed malignant cell states in GCOs had increased fidelity to cell states in patient samples, highlighting the importance of the neuroglial TME in influencing GBM expression programs. Most strikingly, we observed widespread transfer of reporter proteins/mRNA and endogenous mRNA from malignant to nonmalignant cells. This transfer was mediated by EVs with an observed bias for source cells of AC/MES-like malignant cells and target cells of oRG/astroglia nonmalignant types. Together, these results highlight the value of modeling GBM in a heterogeneous, functionally integrated context.

Although the extent to which GFP protein or RNA molecules were transferred from malignant to multiple nonmalignant cell populations in our model may seem surprising, it is not without precedent. For example, in a series of *in vivo* studies, functional GFP-labeled photoreceptors were transplanted into damaged host retinae, with improved visual function resulting primarily from cell-to-cell material transfer (39, 40). In oncology, this phenomenon has been less appreciated: reporter labeling is invariably used for high-confidence identification of malignant cell populations across common experimental models, although there are documented cases of intercellular transfer involving tumor-associated immune populations (41). Moving forward, the potential for unexpected (and biologically relevant) intercellular transfer must be carefully considered, particularly with increasingly integrated tumor models and sophisticated measurement techniques.

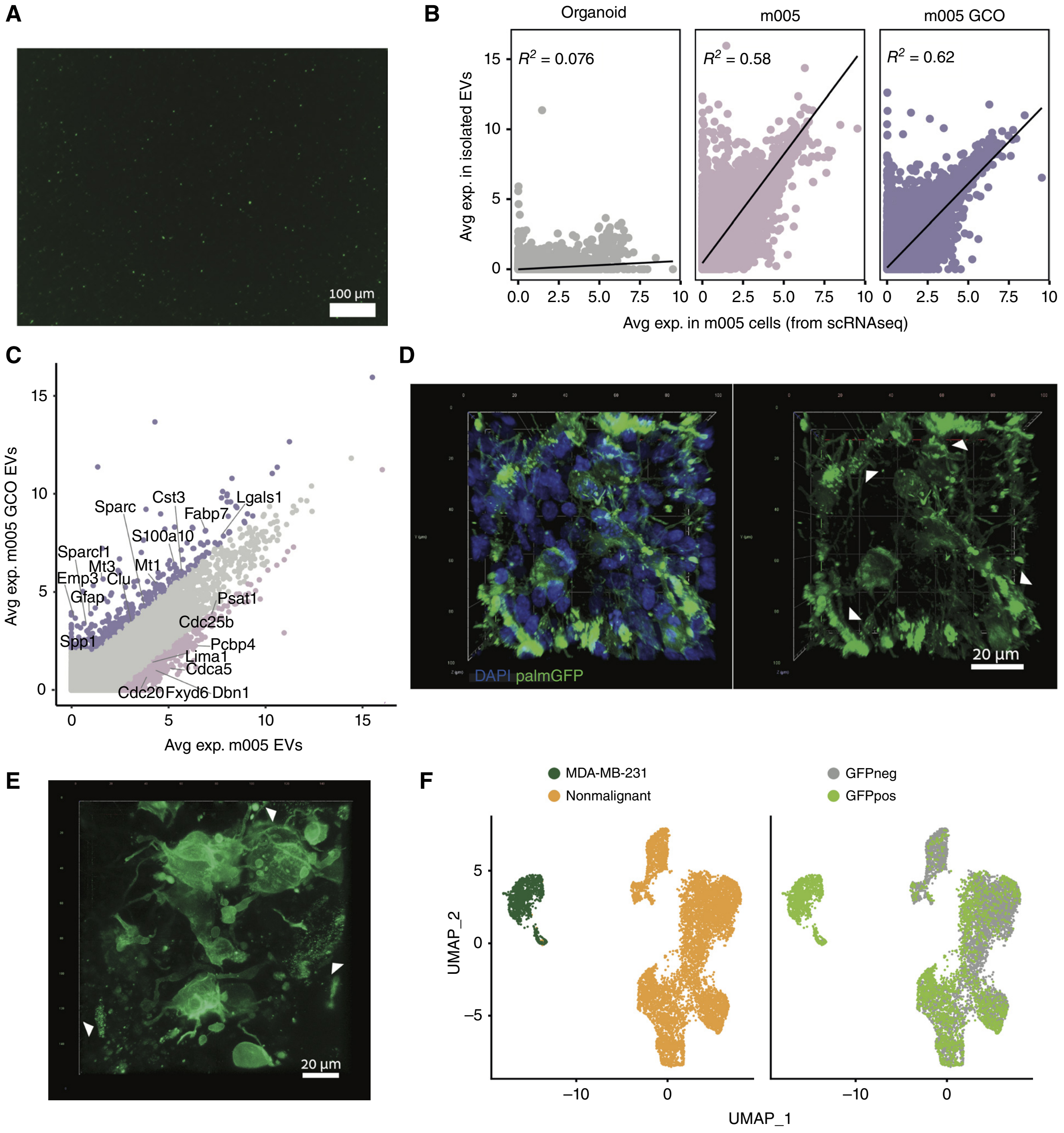

Figure 5. EVs mediate intercellular transfer in GCOs. **A,** Fluorescence microscopy of purified EVs from MGG23-GFP cells. **B,** Scatterplots showing correlation between expression of malignant transcripts in EVs isolated from cortical organoids (left), m005-GFP cells (center), and m005 GCOs (right; *y* axis) and malignant transcripts from m005 single cells in GCOs (*x* axis). **C,** Scatterplot shows expression of genes in EVs from m005 GCOs (*y* axis) compared with m005 cells (*x* axis). The genes colored are the genes with highest residuals from the linear fit. **D,** Confocal imaging of fixed sections (~50 microns) from m005-palmGFP GCOs. Arrowheads show regions in which vesicles are contained within membrane projections. **E,** Live, confocal imaging of MGG23-palmGFP GCOs. Arrowheads show regions of EV accumulation in the TME. **F,** UMAP visualization of scRNA-seq data from an MDA-MB-231 (breast cancer) carcinoma cortical organoid model. Left, cells are colored by identity. Right, cells are colored by GFP-sorting compartment. Avg exp., average expression; DAPI, 4′,6-diamidino-2-phenylindole.

Certainly, organoids may be uniquely well situated for dissecting these phenomena, as they combine *in vitro* ease of manipulation with *in vivo* complexity.

Using GFP-transfer as a facile label for crosstalk, we further uncovered extensive (in terms of the number of transcript species) transfer of endogenous malignant transcripts to nonmalignant cells. Our results may provide one possible additional mechanistic explanation for the observation that GBM-associated macrophages acquire a mesenchymal state that is similar to the MES-like state of malignant GBM cells (9). More broadly, recent large-scale, pan-cancer transcriptome analyses have highlighted that similar expression

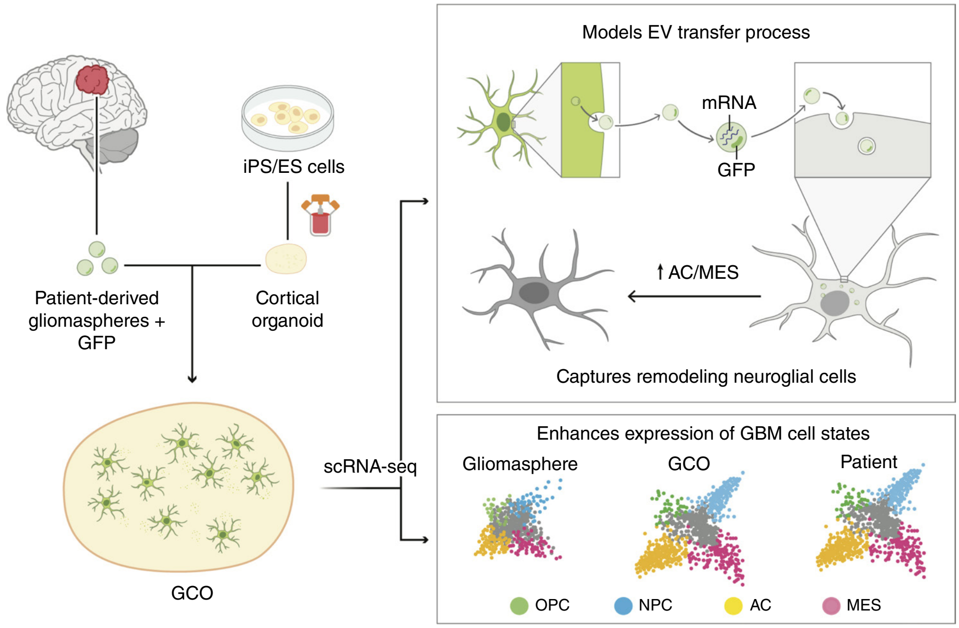

Figure 6. Diagram of the GCO system and findings.

programs are often observed across multiple cell types (both malignant and nonmalignant) within the same tumor (29). Accordingly, we were able to recreate GFP transcript transfer in a breast cancer-cortical organoid model for brain metastasis, suggesting that our results reflect a more fundamental mechanism that is not restricted to glioma. Altogether, these findings suggest that nonmalignant cells in the TME might be remodeled by malignant cells to a greater extent than previously appreciated.

For glioma in particular, we found that GFP-coupled transfer was strongly biased toward AC/MES-like malignant programs. Our data are consistent with recent work suggesting that AC/MES-like malignant cells generate an interconnected tumor cell network with astrocytes (7); in this study, we extend this pattern of connectivity to include numerous RNA species and nonmalignant populations. Importantly, other recent *in vivo* studies in glioma have demonstrated transfer of biomolecules between glioma cells and nonmalignant cells (particularly astrocytes) in the TME, corroborating that our findings in this study likely extend beyond *in vitro* models (42, 43). Although we show that neuronal populations also receive many different malignant transcripts, the functional consequences of this transfer, particularly as they relate to trends in cancer neuroscience, remain to be assessed.

EVs are a conserved mechanism for intercellular communication across cancer and noncancer cell types (33), and we show that they play an important role in mRNA transfer in GCOs. We further observe that the transfer is dependent on malignant cells being directly integrated within the TME, suggesting a possible synergistic influence of the tumor cell network on EV-mediated communication. Indeed, whereas large cargo such as microvesicles or GFP protein/mRNA would not be expected to pass through the gap junction coupling of tumor microtubes, similar and coregulated structures such as open-ended TNTs could be implicated in this transfer (44–46). Further dissection of the relative contributions of each of these processes is significantly limited by a lack of robust methods to perturb EV and TNT pathways. Importantly, the universality of these communication mechanisms would explain the extension of our findings to nonglioma cancer types and related organoid models.

In conclusion, our work contributes three major advances. First, we extend GBM organoid models to include a more complete spectrum of malignant cell states and nonmalignant cell types. Second, we show frequent GFP transfer from malignant to nonmalignant cells in GBM organoids (through protein and/or RNA), demonstrating a functionally integrated TME. Third, we use GFP tracking to illustrate widespread transfer of malignant transcripts to nonmalignant cells through EVs, which may exemplify more general principles of crosstalk in the cancer microenvironment. Future work will extend these findings to patient tumors and explore the long-term functional consequences of this transfer.

METHODS

Experimental Models

GBM and Carcinoma Cell Lines. Primary tumor cultures were derived from surgical samples after obtaining preoperative consent according to Institutional Review Board protocol Dana-Farber/Harvard Cancer Center 10-417. Patient-derived human GBM neurospheres (MGG23, MGG75, MGH143, MGG87, MGG123, MGG101, MGG65, MGG70, and MGG125) were established from tumors and maintained in Neurobasal Medium (Thermo Fisher Scientific) supplemented with 1/2 × N2 and 1 × B27 (Thermo Fisher Scientific), 1% penicillin/streptomycin (Thermo Fisher Scientific), 1.5 × Glutamax (Thermo Fisher Scientific), 20 ng/mL of EGF, and 20 ng/mL of FGF2 (Shenandoah Biotechnology; refs. 3, 47). Mouse (m005) GBM cell lines were obtained from the Salk Institute and maintained in semi-adherent culture in DMEM/F12 (Corning) supplemented with 1 × N2 (Thermo Fisher Scientific), 1 × L-Glutamine (Corning), antibiotic–antimycotic (Thermo Fisher Scientific), 40 μg/mL heparin (Sigma-Aldrich), 20 ng/mL of EGF, and 20 ng/mL of FGF2 (Shenandoah Biotechnology; ref. 48).

MDA-MB-231 cells (RRID: CVCL_0062) were obtained from the ATCC and maintained in adherent culture in DMEM (Corning) supplemented with 10% FBS. Cell lines were routinely tested and found negative for *Mycoplasma*.

Pluripotent Stem Cell Culture. All experiments involving human cells were performed according to the International Society for Stem Cell Research (ISSCR) 2016 guidelines and approved by the Harvard University Institutional Review Board and Embryonic Stem Cell Research Oversight (ESCRO) committees. The 11a iPSC line (RRID: CVCL_8987) was obtained from the Harvard Stem Cell Institute. The PGP1 iPSC line was derived from the laboratory of G. Church (Church, G.M., 2005; RRID: CVCL_F182). The H1 hESC line (also known as WA01; RRID: CVCL_9771) was purchased from WiCell. The cells were cultured on Geltrex-coated dishes (Gibco) in mTeSR1 medium (Stem Cell Technologies) supplemented with 100 U/mL penicillin and 100 μg/mL streptomycin and maintained at 37°C in 5% CO_2. Cell cultures were routinely tested and found negative for *Mycoplasma* and were karyotypically normal. PGP1 and H1 cell lines were authenticated using short tandem repeat analysis completed by TRIPath (2018) and WiCell (2021), respectively. For authentication of the 11a cell line, refer to Quadrato and colleagues (49).

Cortical Organoid Differentiation. Cortical organoids were generated as previously described (25). On day 0, human PSC cells were dissociated into single cells with Accutase (Gibco), and 9,000 cells were seeded per well of an ultra-low cell adhesion 96-well plate (sBio PrimeSurface plate; Sumitomo Bakelite) in Cortical Differentiation Medium (CDM) I, composed of Glasgow minimum essential medium (Gibco), 20% KnockOut Serum Replacement (Gibco), 0.1 mmol/L minimum essential medium nonessential amino acids (Gibco), 1 mmol/L pyruvate (Gibco), 0.1 mmol/L 2-mercaptoethanol (Gibco), 100 U/mL penicillin, and 100 μg/mL streptomycin (Corning). From days 0 to 18, CDM I was supplemented with Wnt inhibitor IWR1 (Calbiochem, 3 μmol/L) and TGFb inhibitor SB431542 (Stem Cell Technologies, 5 μmol/L). On day 18, the aggregates were transferred to ultra-low attachment culture dishes (Corning) and cultured under orbital agitation (80 rpm) in CDM II containing DMEM/F12 medium (Gibco), 2 mmol/L Glutamax (Gibco), 1% N2 (Gibco), 1% Chemically Defined Lipid Concentrate (Gibco), 0.25 μg/mL Fungizone (Gibco), 100 U/mL penicillin, and 100 μg/mL streptomycin. On day 35, the aggregates were transferred to spinner-flask bioreactors (Corning) and maintained in CDM III [DMEM/F12 medium (Gibco), 10% FBS (GE-Healthcare), 2 mmol/L Glutamax (Gibco), 1% N2 (Gibco), 1% Chemically Defined Lipid Concentrate (Gibco), 5 μg/mL heparin (Sigma), 1% Matrigel (Corning), 0.25 μg/mL Fungizone (Gibco), 100 U/mL penicillin, and 100 μg/mL streptomycin]. From day 70 onward, the organoids were cultured in CDM IV [CDM III supplemented with 2% B27 supplement (Gibco) and 2% Matrigel (Corning)].

Method Details

Establishment of GCOs. GCO establishment procedures were approved according to Mass General Brigham Institutional Biosafety Committee (IBC) protocol #2014B000089. Long-term cultured cortical organoids (~4–6 months post-differentiation) were transferred to ultra-low attachment 6-well plates (Corning), with up to five organoids per well, prior to coculture with GBM cells. Cortical organoids were maintained in CDM IV without Matrigel (49). Separately, GFP- or tdT- tagged GBM cells were dissociated using TrypLE (Thermo Fisher Scientific) into single-cell suspensions. GBM cells were centrifuged at 300 relative centrifugal force (RCF) and resuspended in CDM IV (without Matrigel) at a concentration of approximately one million cells per mL. To initiate coculture of GBM cells and cortical organoids, ~250,000 to 400,000 GBM cells in CDM IV were added to each well of a 6-well plate containing 5 organoids each, with a total volume of ~2 to 2.5 mL media per well. Cocultures in six-well plates were subsequently kept on a shaker in a 37°C/5% CO_2 incubator (Thermo Fisher Scientific) at 88 to 95 RPM for 24 hours, during which time the cell suspension was regularly triturated (every ~4–6 hours) with a P1000 pipet. Trituration was carried out to maintain a single-cell suspension of GBM cells and periodically reorient cortical organoids within the well. Cultures were periodically checked under a fluorescent microscope during this 24-hour period to ensure uniform single-cell engraftment of GFP/tdT-positive cells into cortical organoids. After 24 to 48 hours and successful engraftment, cortical organoids were washed with CDM IV (without Matrigel) (to remove unattached gliomaspheres) and replated in a different low-attachment six-well plate with CDM IV (without Matrigel) for prolonged culture at 37°C/5% CO_2 with shaking (88–95 RPM). During prolonged culture, CDM IV (without Matrigel) media was replaced every ~2 days. Established GCOs were maintained for 2 weeks prior to dissociation, FACS, and scRNA-seq.

Single-Cell Dissociation of Organoids. Individual cortical and GCOs were dissociated into single-cell suspensions using Worthington Papain Dissociation System Kit (Worthington Biochemical). A detailed description of the dissociation protocol is available at Protocol Exchange (https://doi.org/10.21203/RS.2.9542/V1).

FACS of GFP/tdT-Positive and -Negative Populations. Dissociated organoids were pooled together by model and resuspended in ice cold PBS with 1% BSA for FACS. Each sample was co-stained for 30 minutes with CellTrace Calcein Violet, AM (Thermo Fisher Scientific) and TO-PRO-3 (Thermo Fisher Scientific) live and dead cell markers, respectively. For each GCO FACS experiment, an age and batch matched cortical organoid was run as a negative gating control. GFP/tdT-positive and -negative fractions from each model were collected into separate 1.5-mL microcentrifuge tubes, with a minimum goal of 25,000 cells per collection tube. Sorting was performed with a FACS Aria Fusion Special Order System (Becton Dickinson). The sorting was limited to less than 90 minutes per sample, and the collection tubes were maintained at 4°C for the sort duration, to minimize FACS-processing artifacts on the downstream scRNA-seq results. Sorted, viable cell populations were immediately transferred to droplet-based (10x) scRNA-seq pipelines.

For Smart-seq2 experiments, individual cells were directly sorted into 96-well plates containing TCL buffer (QIAGEN) with 1% β-mercaptoethanol. The plates were frozen on dry ice immediately after sorting and stored at −80°C prior to whole-transcriptome amplification, library preparation, and sequencing.

scRNA-Seq. For the 10X experiments, GFP/tdT-positive and -negative pools were centrifuged at 250 RCF for 5 minutes, and the resulting cell pellets were resuspended in PBS +0.04% BSA at a target concentration of one million cells per mL. The scRNA-seq libraries were generated using the Chromium Next GEM Single Cell 3′ GEM, Library & Gel Bead Kit v3.1, Chromium Next GEM Chip G, and 10x Chromium Controller (10x Genomics) according to the 10X Single Cell 3′ v3.1 protocol. The GFP/tdT positive and negative cell populations were separately profiled for each GCO model. We loaded approximately 10,000 single cells to the Chromium Controller with a targeted recovery of 6,000 cells per cell population. Single cells, reagents and single gel beads containing barcoded oligonucleotides were encapsulated into nanoliter-sized droplets and subjected to reverse transcription. Droplets were broken and the barcoded cDNAs were purified with DynaBeads and amplified by 12 cycles of

PCR [98°C for 3 minutes; (98°C for 15 seconds, 63°C for 20 seconds, 72°C for 1 minute) × 12; 72°C for 1 minute]. 3′ gene expression cDNA were size-selected and separated with SPRIselect Reagent (Beckman Coulter), and then fragmented, end-repaired, ligated with index adapters. Quality control of the resulting libraries was performed with the Bioanalyzer High Sensitivity DNA Analysis (Agilent). The constructed gene expression libraries were paired-end sequenced using a NextSeq 2000 sequencer (Illumina).

Smart-seq2 whole transcriptome amplification, library construction, and sequencing were performed as previously published (3).

In vitro Labeling of Cell Lines with GFP/tdT Lentiviruses. GFP and tdT lentiviruses were packaged with pLV-CMV-eGFP and pLV-CAG-tdTomato transgenic vectors, respectively, using a third generation lentiviral packaging system in 293T cells (RRID: CVCL_0063). Lentiviral particles were collected, precipitated, and concentrated using lentiviral precipitation solution (Alstem). Concentrated lentiviral particles (without polybrene) were directly added to gliomasphere cells (dissociated with TrypLE) in six-well plates, and the media was replaced after 48 hours. Cells were allowed to expand for several weeks, after which GFP/tdT-positive cells were purified with FACS as needed, and the resulting cell cultures were used for subsequent experiments or cryopreserved as stocks in liquid nitrogen.

Immunohistochemistry and Microscopy. GCO samples were fixed in 4% paraformaldehyde (PFA) at room temperature overnight, washed with PBS, and then dehydrated in 30% sucrose in PBS at 4°C overnight. Cryoprotected samples were subsequently embedded in freshly prepared bovine gelatin solution (5 g bovine gelatin, 3.75 g sucrose, in 25 mL PBS) in plastic cryomolds. After gelatin polymerization for 20 minutes at room temperature, embedded organoids were flash frozen in a dry ice and ethanol bath. Frozen sections were cryosectioned at 15 to 50 micron thickness, and sections were added to slides for long-term storage at −80°C. Sections were washed with 0.1% Triton X-100 in PBS, blocked for 1 hour at room temperature with 5% donkey serum + 0.1% Triton X-100 in PBS, and incubated overnight with primary antibody (anti-human mitochondria; Abcam 113-1; RRID: AB_2332217) in 2.5% donkey serum + 0.1% Triton X-100 in PBS. After washing, sections were incubated with secondary antibodies in 2.5% donkey serum + 0.1% Triton X-100 in PBS for 1 hour at room temperature. Secondary antibodies were washed with PBS + 0.1% Triton X-100, and incubated with 4′,6-diamidino-2-phenylindole (DAPI; 1 μg/mL in PBS) for 15 minutes. The samples were mounted with a coverslip and Fluoromount mounting medium for long-term storage and imaging. Confocal images were acquired with a Zeiss LSM 800 with Airyscan and analyzed using ZEN (Zeiss) imaging software.

Isolation and Characterization of Extracellular Vesicles (EV). GBM cell lines, GCO models, and cortical organoids were cultured as described previously. After 1 week of continuous culture, conditioned media was collected and centrifuged at 300 RCF to remove cell debris. Conditioned media was concentrated with an Amicon Ultra-15 100K MWCO filter (Millipore) at 600 RCF for 30 minutes. Concentrated samples were loaded onto qEV original SEC columns (IZON Sciences) and 13 fractions (500 μL each) were collected by elution with PBS using the Automatic Fraction Collector according to the manufacturer's protocol. Fractions 7 through 11, containing EVs, were further concentrated with a 100kDa MWCO spin filter (Millipore); RNPs that carry RNA were contained in fractions 12 and beyond, and subsequently discarded. For further characterization, EV samples were diluted 200X in PBS and analyzed with nanoparticle tracking analysis (NTA) on a NanoSight LM10 (Salisbury, UK) according to manufacturer's instructions. For each measurement, five 1-minute videos were captured, after which videos were analyzed by the in-built NanoSight Software NTA 3.2 to determine nanoparticle (EV) size distributions and concentrations.

Library Preparation and Sequencing of Extracted EV mRNA. Purified EVs were loaded onto exoRNeasy MIDI columns (QIAGEN) to extract total RNA. Total RNA was quantified and sequencing libraries were constructed using a Smart-Seq2 protocol with reagents adapted to accommodate bulk-EV RNA (3 ng total RNA per sample) as input. Sequencing libraries had selective amplification of mRNAs through the presence of oligo(dT)-tailed primers in the Smart-Seq2 protocol. Quality control of the resulting libraries was performed with the Bioanalyzer High Sensitivity DNA Analysis (Agilent). The constructed gene expression libraries were paired-end sequenced using a NextSeq 2000 sequencer (Illumina).

Cortical Organoid Coculture Experiments. 11A-derived cortical organoids (~4 months post-differentiation) were plated in low-attachment six well plates (one organoid per well) and cultured with CDM IV media, without Matrigel, as described in the GCO establishment protocol. All coculture conditions, subsequently described, were carried out for 1 week on a shaker (95 RPM) at 37C/5% CO_2, with media changes every 2 days, after which cortical organoids were dissociated (as described previously) into single cells and analyzed on a Cytek Aurora flow cytometer. (i) Purified EVs: 50 μL of purified EVs (1.6E11 particles/mL) were added directly to cortical organoid culture media, every 2 days for the duration of the experiment. (ii) Conditioned media: conditioned media from m005-GFP cells was filtered (0.45 micron) and frozen, with 1:2 conditioned media to CDM IV added at each media change for the cortical organoids. (iii) Transwell culture: m005-GFP cells (100k cells per insert) were plated on a hanging transwell insert (0.4 micron, Millipore), which was subsequently inserted into a six-well plate with a cortical organoid in CDM IV media. The transwell insert was carefully maintained for the duration of the experiment. (iv) Controls: 11A cortical organoids, m005-GFP cells, and m005 GCOs were cultured or initiated as described previously, for the 1-week duration of the experiment.

Live Imaging of GCOs. MGG23-palmGFP GCOs were established and cultured for 1 week, as previously described. GCOs were plated in a 96-well glass bottom plate, and embedded in Matrigel (Corning) for 2 hours, prior to imaging on a Zeiss LSM800 Airyscan with an environmental control chamber.

Data Analysis

scRNA-Seq Data Processing. Raw data were processed using 10x CellRanger pipeline to output filtered count matrices. Cells were aligned to a custom genome that was created by adding the GFP sequence (Supplementary Data) to the human and mouse genomes using cellranger mkref to quantify the GFP reads per cell. Next, as quality control, we excluded cells with fewer than 1,000 detected genes. Among the remaining cells, we detected on average of 4,058 genes per cell. Expression levels were quantified as $E(i,j) = \log_2[1 + CPM(i,j)/10]$, in which $CPM(i,j)$ refers to $10^6 \times UMI(i,j)/sum[UMI\ 1\ldots n,j]$, for gene i in sample j, with n being the total number of analyzed genes. *CPM* values were divided by 10, as described above for *TPM* values. We defined relative expression over the remaining cells for each study separately by centering the expression levels per gene, $E_{rel}(i,j) = Ei,j - mean[Ei,1\ldots n]$. Next, we calculated the $E_{avg}(i) = \log_2[mean(CPMi,1\ldots n)+1]$ for each gene and excluded genes with $E_{avg} < 4$.

Definition of Gene Signature Scores. Cells or bulk tumors were scored for a gene signature as previously described using the R package scalop (https://github.com/jlaffy/scalop). Given a set of genes (Gj) reflecting an expression signature of a specific cell type or biological function, we calculate for each cell i, a score, $SCj\ (i)$, quantifying the relative expression of Gj in cell i, as the average relative expression (Er)

of the genes in Gj, compared with the average relative expression of a control gene set (Gj cont): $SCj\,(i) = average[Er(Gj,i)] - average[Er(Gj\ cont,i)]$. The control gene set is defined by first binning all analyzed genes into 30 bins of aggregate expression levels (Ea) and then, for each gene in the gene set Gj, randomly selecting 100 genes from the same expression bin. In this way, the control gene set has a comparable distribution of expression levels to that of Gj, and the control gene set is 100-fold larger, such that its average expression is analogous to averaging over 100 randomly selected gene sets of the same size as the considered gene set. Cells were scored for each study separately.

Assignment of Cell Types. The gene cell matrix underwent dimension reduction using UMAP and Louvain clustering using the R package Seurat (https://satijalab.org/seurat/). To define malignant cells, we inferred CNAs from single-cell data, as previously described. Malignant cells were assigned to the meta-module with the highest score between the six meta-modules (MES1-like, MES2-like, NPC1-like, NPC2-like, AC-like, and OPC-like), as previously described [Neftel and colleagues (3)]; however, cells with a score of less than 0.3 for any program or a difference of less than 0.1 between the highest and second-highest state scores were defined “unclassified.” For most analyses, we collapsed the MES1 and MES2 groups of cells into one group of MES-like cells, and similarly, the NPC1 and NPC2 cells into one group of NPC-like cells. Nonmalignant cells were assigned in a similar matter using gene signatures for the defined cell types as defined in (Velasco and colleagues) (25). For the m005 mouse GBM cells, cells were assigned in the same method but using the *de novo* NMF programs (described below) instead of the Neftel GBM states.

Characterization and Comparison of Malignant Cells to Human Transcriptional Heterogeneity. For the malignant cells [from both human and mouse (m005) origin], we analyzed each cell line separately to identify patterns of expression heterogeneity. NMF was applied to the Er values by transforming all negative values to zero. We performed NMF using the R package NMF with the number of factors k = 6–9 and defined expression programs as the top 50 genes (by NMF score). For the human malignant cells, we clustered all of the generated NMF programs to define metaprograms, as previously described (28, 29), which we refer to in the text as *de novo* programs. Programs of expression heterogeneity in human GBM were previously defined: MES1-like, MES2- like, NPC1-like, NPC2-like, AC-like, OPC-like, G1S, and G2M [Neftel and colleagues (3)]. For the human metaprograms and m005 *de novo* programs defined, we annotated each one based on the maximum similarity with each of the Neftel human programs.

Comparing Transcriptional Heterogeneity to In Vitro Data. For each of the cell lines grown in cortical organoids, we also have generated data in *in vitro* gliomasphere conditions. To compare the robustness of the human GBM cellular states between *in vitro* and organoid conditions, we scored the malignant cells for each cell line for the cellular states for each condition separately. We plotted the scores, colored by cell assignment using star plots, as previously described [Neftel and colleagues (3)]. In addition, we quantified the difference in magnitude of the cell states by plotting the score of the metaprogram which a cell was assigned to in each condition (boxplot). Additionally, we conducted the same analysis comparing the GCO system to GBM cells cultured *in vitro*, tumor organoids, and cerebral organoid from an external dataset from Pine and colleagues (23).

Assignment of Each Cell Species of Origin in the Species-Mismatch Experiment. Cells were aligned to a concatenated human and mouse genome. Then for each cell, the number of human genes that were detected was plotted against the number of mouse genes detected. Cells were assigned to a species if there was 10 times more genes from one species compared with another and at least 1,000 genes detected.

Detection of Transferred Transcripts. To identify transferred genes, we used two approaches: in the species-mismatch experiment, mouse genes that were detected in the human organoid cells were considered transferred. In the human GBM cell line experiments, we estimated the genes transferred by selecting the genes with the highest residual gene expression when comparing the average expression in malignant cells versus nonmalignant organoid cells.

Analysis of EV Transcripts. Purified EVs were subjected to bulk RNA-seq to profile their transcriptomic content, as described previously. We evaluated the correlation between the pseudobulk gene expression data from malignant m005 cells (obtained from scRNA-seq data) and the transcript levels in the EVs. This allowed us to determine the similarity between the gene expression profiles of the malignant cells and the transcripts found in the isolated EVs. Finally, to identify genes specifically transferred within the m005 GCO system, we compared the transcript profiles of m005 EVs and m005 GCO EVs. We computed the residuals from this comparison, focusing on genes with the highest residuals to highlight those with differential transfer between the two EV sources.

Data Availability

Data generated in this study are publicly available in Gene Expression Omnibus (RRID: SCR_005012) at GSE276838. All code generated in this study are publicly available at https://github.com/rchanoch/Glioblastoma-cortical-organoids.

Authors’ Disclosures

V. Mangena reports a patent for US20230324371A1 pending. B. Paulsen reports being currently employed by Gameto, Inc. X.O. Breakefield reports grants from the NIH during the conduct of the study. A. Regev reports other support from Howard Hughes Medical Institute during the conduct of the study and personal fees and other support from Celsius Therapeutics, personal fees from ThermoFisher Scientific, and personal fees and other support from Immunitas outside the submitted work; in addition, A. Regev has a patent for “Single-cell genomics methods” pending, issued, and licensed and a patent for “Spatial genomics methods” pending and issued and is an employee of Genentech and has equity in Roche. P. Arlotta reports grants from Stanley Center for Psychiatric Research and grants from the NIH during the conduct of the study and nonfinancial support from Foresite Labs, Vesalius Therapeutics, and CNSII outside the submitted work; in addition, P. Arlotta has a patent for “*Ex vivo* brain tumor model” pending. I. Tirosh reports personal fees from Immunitas Therapeutics outside the submitted work. M.L. Suvà reports grants from the NIH, the Mark Foundation, the Sontag Foundation, and the Broad Institute–ISF during the conduct of the study and personal fees from Immunitas Therapeutics outside the submitted work; in addition, M.L. Suvà has a patent for U.S. provisional patent application No. 63/064,905 filed by the Broad Institute entitled “*Ex vivo* brain tumor model” pending. No disclosures were reported by the other authors.

Authors’ Contributions

V. Mangena: Conceptualization, formal analysis, investigation, methodology, writing–original draft, writing–review and editing. **R. Chanoch-Myers:** Conceptualization, data curation, software, formal analysis, visualization, methodology, writing–original draft, writing–review and editing. **R. Sartore:** Resources, investigation, writing–review and editing. **B. Paulsen:** Resources, investigation, writing–review and editing. **S. Gritsch:** Investigation, writing–review and editing. **H. Weisman:** Investigation, writing–review and editing. **T. Hara:** Resources, investigation, writing-review and editing. **X.O. Breakefield:** Resources, writing–review and editing. **K. Breyne:**

Resources, investigation, writing–review and editing. **A. Regev:** Conceptualization, supervision, funding acquisition, writing–review and editing. **K. Chung:** Conceptualization, supervision, funding acquisition, writing–review and editing. **P. Arlotta:** Conceptualization, supervision, funding acquisition, writing–review and editing. **I. Tirosh:** Conceptualization, supervision, funding acquisition, writing–original draft, project administration, writing–review and editing. **M.L. Suvà:** Conceptualization, supervision, funding acquisition, writing–original draft, project administration, writing–review and editing.

Acknowledgments

This work was supported by a Broad Institute–Israel Science Foundation Collaborative Project Award (I. Tirosh and M.L. Suvà), the Massachusetts General Hospital (MGH) Research Scholars program (M.L. Suvà), The Mark Foundation Emerging Leader Award (M.L. Suvà), the NIH. R37CA245523 (M.L. Suvà), the NIH. R01CA258763 (M.L. Suvà), the Sontag Foundation Distinguished Scientist Award (M.L. Suvà), the Stanley Center for Psychiatric Research (P. Arlotta), and the NIH. RF1 MH123977 (P. Arlotta). V. Mangena is supported by 5T32CA272386. I. Tirosh is the incumbent of the Drs. Celia Zwillenberg-Fridman and Lutz Zwillenberg Career Development Chai, and is supported by the Zuckerman STEM Leadership Program, the Mexican Friends New Generation, the Benoziyo Endowment Fund, and grants from the Human Frontiers Science Program. X.O. Breakefield is supported by funds from the NCI CA232103. K. Breyne is funded through the NIH-K22CA282019. A. Regev was supported by funds from the Howard Hughes Medical Institute, the Klarman Cell Observatory, the STARR Cancer Consortium, the NCI grant 1U24CA180922, the NCI grant R33CA202820, and Koch Institute support. Confocal imaging was performed in the Microscopy Core of the Program in Membrane Biology, which is partially supported by a Centre for the Study of Inflammatory Bowel Disease Grant DK043351 and a Boston Area Diabetes and Endocrinology Research Center Award DK135043; the Zeiss confocal system is supported by grant S10OD021577-01. We thank Dennis Brown, Richard Bouley, and Diane Capen from the MGH Program in Membrane Biology core for experimental support; the entire Suva and Tirosh laboratories for support and insightful discussions; and Gabrielle Phillips, Meaghan Cruise, Matthew Drummond, and Jeremy Fung in the MGH Pathology flow cytometry core for technical support in cell sorting.

Note

Supplementary data for this article are available at Cancer Discovery Online (http://cancerdiscovery.aacrjournals.org/).

Received November 10, 2023; revised August 27, 2024; accepted October 3, 2024; published first October 7, 2024.

REFERENCES

1. Tan AC, Ashley DM, López GY, Malinzak M, Friedman HS, Khasraw M. Management of glioblastoma: state of the art and future directions. CA Cancer J Clin 2020;70:299–312.
2. Patel AP, Tirosh I, Trombetta JJ, Shalek AK, Gillespie SM, Wakimoto H, et al. Single-cell RNA-seq highlights intratumoral heterogeneity in primary glioblastoma. Science 2014;344:1396–401.
3. Neftel C, Laffy J, Filbin MG, Hara T, Shore ME, Rahme GJ, et al. An integrative model of cellular states, plasticity, and genetics for glioblastoma. Cell 2019;178:835–49.e21.
4. Garofano L, Migliozzi S, Oh YT, D'Angelo F, Najac RD, Ko A, et al. Pathway-based classification of glioblastoma uncovers a mitochondrial subtype with therapeutic vulnerabilities. Nat Cancer 2021;2:141–56.
5. Couturier CP, Ayyadhury S, Le PU, Nadaf J, Monlong J, Riva G, et al. Single-cell RNA-seq reveals that glioblastoma recapitulates a normal neurodevelopmental hierarchy. Nat Commun 2020;11:3406.
6. Müller S, Liu SJ, Di Lullo E, Malatesta M, Pollen AA, Nowakowski TJ, et al. Single-cell sequencing maps gene expression to mutational phylogenies in PDGF- and EGF-driven gliomas. Mol Syst Biol 2016;12:889.
7. Venkataramani V, Yang Y, Schubert MC, Reyhan E, Tetzlaff SK, Wißmann N, et al. Glioblastoma hijacks neuronal mechanisms for brain invasion. Cell 2022;185:2899–917.e31.
8. Bhaduri A, Di Lullo E, Jung D, Müller S, Crouch EE, Espinosa CS, et al. Outer radial glia-like cancer stem cells contribute to heterogeneity of glioblastoma. Cell Stem Cell 2020;26:48–63.e6.
9. Hara T, Chanoch-Myers R, Mathewson ND, Myskiw C, Atta L, Bussema L, et al. Interactions between cancer cells and immune cells drive transitions to mesenchymal-like states in glioblastoma. Cancer Cell 2021;39:779–92.e11.
10. Venkatesh HS, Morishita W, Geraghty AC, Silverbush D, Gillespie SM, Arzt M, et al. Electrical and synaptic integration of glioma into neural circuits. Nature 2019;573, 539–45.
11. Osswald M, Jung E, Sahm F, Solecki G, Venkataramani V, Blaes J, et al. Brain tumour cells interconnect to a functional and resistant network. Nature 2015;528:93–8.
12. Venkataramani V, Tanev DI, Strahle C, Studier-Fischer A, Fankhauser L, Kessler T, et al. Glutamatergic synaptic input to glioma cells drives brain tumour progression. Nature 2019;573:532–8.
13. Siolas D, Hannon GJ. Patient-derived tumor xenografts: transforming clinical samples into mouse models. Cancer Res 2013;73:5315–19.
14. Katt ME, Placone AL, Wong AD, Xu ZS, Searson PC. In vitro tumor models: advantages, disadvantages, variables, and selecting the right platform. Front Bioeng Biotechnol 2016;4:12.
15. Jacob F, Salinas RD, Zhang DY, Nguyen PTT, Schnoll JG, Wong SZH, et al. A patient-derived glioblastoma organoid model and biobank recapitulates inter- and intra-tumoral heterogeneity. Cell 2020;180: 188–204.e22.
16. LeBlanc VG, Trinh DL, Aslanpour S, Hughes M, Livingstone D, Jin D, et al. Single-cell landscapes of primary glioblastomas and matched explants and cell lines show variable retention of inter- and intratumor heterogeneity. Cancer Cell 2022;40:379–92.e9.
17. Wang X, Sun Y, Zhang DY, Ming G, Song H. Glioblastoma modeling with 3D organoids: progress and challenges. Oxf Open Neurosci 2023;2:kvad008.
18. Klein E, Hau A-C, Oudin A, Golebiewska A, Niclou SP. Glioblastoma organoids: pre-clinical applications and challenges in the context of immunotherapy. Front Oncol 2020;10:604121.
19. da Silva B, Mathew RK, Polson ES, Williams J, Wurdak H. Spontaneous glioblastoma spheroid infiltration of early-stage cerebral organoids models brain tumor invasion. SLAS Discov 2018;23:862–8.
20. Goranci-Buzhala G, Mariappan A, Gabriel E, Ramani A, Ricci-Vitiani L, Buccarelli M, et al. Rapid and efficient invasion assay of glioblastoma in human brain organoids. Cell Rep 2020;31:107738.
21. Krieger TG, Tirier SM, Park J, Jechow K, Eisemann T, Peterziel H, et al. Modeling glioblastoma invasion using human brain organoids and single-cell transcriptomics. Neuro Oncol 2020;22:1138–49.
22. Linkous A, Balamatsias D, Snuderl M, Edwards L, Miyaguchi K, Milner T, et al. Modeling patient-derived glioblastoma with cerebral organoids. Cell Rep 2019;26:3203–11.e5.
23. Pine AR, Cirigliano SM, Nicholson JG, Hu Y, Linkous A, Miyaguchi K, et al. Tumor microenvironment is critical for the maintenance of cellular states found in primary glioblastomas. Cancer Discov 2020;10: 964–79.
24. Ogawa J, Pao GM, Shokhirev MN, Verma IM. Glioblastoma model using human cerebral organoids. Cell Rep 2018;23:1220–9.
25. Velasco S, Kedaigle AJ, Simmons SK, Nash A, Rocha M, Quadrato G, et al. Individual brain organoids reproducibly form cell diversity of the human cerebral cortex. Nature 2019;570:523–7.
26. Tirosh I, Venteicher AS, Hebert C, Escalante LE, Patel AP, Yizhak K, et al. Single-cell RNA-seq supports a developmental hierarchy in human oligodendroglioma. Nature 2016;539:309–13.
27. Uzquiano A, Kedaigle AJ, Pigoni M, Paulsen B, Adiconis X, Kim K, et al. Proper acquisition of cell class identity in organoids allows definition of fate specification programs of the human cerebral cortex. Cell 2022;185:3770–88.e27.

28. Kinker GS, Greenwald AC, Tal R, Orlova Z, Cuoco MS, McFarland JM, et al. Pan-cancer single-cell RNA-seq identifies recurring programs of cellular heterogeneity. Nat Genet 2020;52:1208–18.
29. Gavish A, Tyler M, Greenwald AC, Hoefflin R, Simkin D, Tschernichovsky R, et al. Hallmarks of transcriptional intratumour heterogeneity across a thousand tumours. Nature 2023;618:598–606.
30. Warren A, Chen Y, Jones A, Shibue T, Hahn WC, Boehm JS, et al. Global computational alignment of tumor and cell line transcriptional profiles. Nat Commun 2021;12:22.
31. Sofroniew MV, Vinters HV. Astrocytes: biology and pathology. Acta Neuropathol 2010;119:7–35.
32. Zamanian JL, Xu L, Foo LC, Nouri N, Zhou L, Giffard RG, et al. Genomic analysis of reactive astrogliosis. J Neurosci 2012;32:6391–410.
33. Zaborowski MP, Balaj L, Breakefield XO, Lai CP. Extracellular vesicles: composition, biological relevance, and methods of study. Bioscience 2015;65:783–97.
34. Abels ER, Breakefield XO. Introduction to extracellular vesicles: biogenesis, RNA cargo selection, content, release, and uptake. Cell Mol Neurobiol 2016;36:301–12.
35. O'Brien K, Breyne K, Ughetto S, Laurent LC, Breakefield XO. RNA delivery by extracellular vesicles in mammalian cells and its applications. Nat Rev Mol Cell Biol 2020;21:585–606.
36. Lai CP, Kim EY, Badr CE, Weissleder R, Mempel TR, Tannous BA, et al. Visualization and tracking of tumour extracellular vesicle delivery and RNA translation using multiplexed reporters. Nat Commun 2015;6:7029.
37. Dupont M, Souriant S, Lugo-Villarino G, Maridonneau-Parini I, Vérollet C. Tunneling nanotubes: intimate communication between myeloid cells. Front Immunol 2018;9:43.
38. Chakraborty R, Nonaka T, Hasegawa M, Zurzolo C. Tunnelling nanotubes between neuronal and microglial cells allow bi-directional transfer of α-Synuclein and mitochondria. Cell Death Dis 2023;14:329.
39. Kalargyrou AA, Basche M, Hare A, West EL, Smith AJ, Ali RR, et al. Nanotube-like processes facilitate material transfer between photoreceptors. EMBO Rep 2021;22:e53732.
40. Pearson RA, Gonzalez-Cordero A, West EL, Ribeiro JR, Aghaizu N, Goh D, et al. Donor and host photoreceptors engage in material transfer following transplantation of post-mitotic photoreceptor precursors. Nat Commun 2016;7:13029.
41. van der Vos KE, Abels ER, Zhang X, Lai C, Carrizosa E, Oakley D, et al. Directly visualized glioblastoma-derived extracellular vesicles transfer RNA to microglia/macrophages in the brain. Neuro Oncol 2016;18:58–69.
42. Watson DC, Bayik D, Storevik S, Moreino SS, Sprowls SA, Han J, et al. GAP43-dependent mitochondria transfer from astrocytes enhances glioblastoma tumorigenicity. Nat Cancer 2023;4:648–64.
43. Gao X, Zhang Z, Mashimo T, Shen B, Nyagilo J, Wang H, et al. Gliomas interact with non-glioma brain cells via extracellular vesicles. Cell Rep 2020;30:2489–500.e5.
44. Zurzolo C. Tunneling nanotubes: reshaping connectivity. Curr Opin Cell Biol 2021;71:139–47.
45. Winkler F, Wick W. Harmful networks in the brain and beyond. Science 2018;359:1100–1.
46. Pinto G, Saenz-De-Santa-Maria I, Chastagner P, Perthame E, Delmas C, Toulas C, et al. Patient-derived glioblastoma stem cells transfer mitochondria through tunneling nanotubes in tumor organoids. Biochem J 2021;478:21–39.
47. Wakimoto H, Mohapatra G, Kanai R, Curry WT Jr, Yip S, Nitta M, et al. Maintenance of primary tumor phenotype and genotype in glioblastoma stem cells. Neuro Oncol 2012;14:132–44.
48. Marumoto T, Tashiro A, Friedmann-Morvinski D, Scadeng M, Soda Y, Gage FH, et al. Development of a novel mouse glioma model using lentiviral vectors. Nat Med 2009;15:110–6.
49. Quadrato G, Nguyen T, Macosko EZ, Sherwood JL, Min Yang S, Berger DR, et al. Cell diversity and network dynamics in photosensitive human brain organoids. Nature 2017;545:48–53.